CFD simulation of flapped rotors

F. Dehaeze
florent.dehaeze@agustawestland.com

CFD Laboratory, School of Engineering
University of Liverpool
Liverpool
UK

Present address: AgustaWestland
Yeovil
UK

K. D. Baverstock
karl.baverstock@agustawestland.com

AgustaWestland
Yeovil
UK

G. N. Barakos
george.barakos@glasgow.ac.uk

CFD Laboratory, School of Engineering
University of Liverpool
Liverpool
UK

Present Address: School of Engineering
University of Glasgow
Glasgow
UK

ABSTRACT

The use of active trailing edge flaps on rotors may lead to performance benefits as well as noise and vibration reduction. In this work, computational fluid dynamics, using the HMB2 solver, is used to assess the effect of the trailing edge flaps on the whole flight domain of a modern main rotor. Starting from a baseline blade design, multiple techniques are demonstrated. The flap is first assessed using 2D pitching aerofoil simulations, followed by dM$d$$t$ simulations, that account for the simultaneous variations of pitch and Mach around the azimuth. It was shown that enhanced lift was obtained while inspection of the moment coefficient showed negative damping for the flap for a limited set of conditions. Due to the 2D formulation, dM$d$$t$ computations are fast to perform and can be used to inform codes predicting the rotor performance. The flap was then assessed in hover, and only allowed for limited improvement in blade performance at high thrust. In forward flight, the flap was actuated at a frequency of 1 per revolution, and was found to have a strong effect on the loads on the retreating side. The effect on the moments was even stronger. The flight envelope of the blade was explored, and clean and flapped cases were compared. The most noticeable changes occur at high and medium thrust. The CFD method was found to be efficient and robust, without any substantial penalties in CPU time, due to the flap modelling, over the tested conditions.

Paper No. 4348. Manuscript received 6 February 2015, revised version received 18 May 2015, accepted 20 May 2015.
This is an adapted version of a paper first presented at 40th The European Rotorcraft Forum hosted by the Royal Aeronautical Society in Southampton, UK, September 2014

https://doi.org/10.1017/S0001924000011404 Published online by Cambridge University Press

NOMENCLATURE

a_∞ free stream speed of sound
c chord length
C_D aerofoil drag coefficient
C_L aerofoil lift coefficient
C_M aerofoil pitching moment coefficient

C_P pressure coefficient, $C_P = \frac{P-P_\infty}{\frac{1}{2}\rho_\infty V_{loc}^2}$

C_Q rotor torque coefficient, $C_Q = \frac{Q}{\frac{1}{2}\rho_\infty \omega^2 \pi R^5}$

C_T rotor thrust coefficient, $C_T = \frac{T}{\frac{1}{2}\rho_\infty \omega^2 \pi R^4}$

$\vec{F}_i, \vec{F}_v$ inviscid and viscous flux vectors

FM rotor figure of merit, $FM = \frac{C_T^{\frac{3}{2}}}{2C_Q}$

k reduced frequency,

$$k = \frac{\omega c}{2V_\infty}$$

k–ω SST Menter's k-ω shear-stress transport[18]
L_m sectional pitching moment loading, measured around the blade pitching axis
L_q sectional to rque along the blade span, around the rotor axis
L_t sectional thrust along the blade span

M^2C_m Mach-scaled sectional pitching moment coefficient (around the blade pitching axis),

$$M^2C_m = \frac{L_m}{\frac{1}{2}\rho_\infty a_\infty^2 c^2}$$

M^2C_n Mach-scaled sectional thrust coefficient, $M2C_n = \frac{L_t}{\frac{1}{2}\rho_\infty a_\infty^2 c}$

M^2C_q Mach-scaled sectional torque coefficient, $M^2C_q = \frac{L_q}{\frac{1}{2}\rho_\infty a_\infty^2 c^2}$

M_H flap hinge moment
M_∞ free stream Mach number
P local pressure
P_∞ free stream pressure
Q rotor torque
r current spanwise location
R rotor radius

Re_∞ Reynolds number based on the free stream velocity: $Re_\infty = \frac{\rho c V_\infty}{\mu_\infty}$

$\mathbf{R}_{i,j,k}$ flux residual at cell (i,j,k)
T rotor thrust
u,v,w velocity components
$\vec{u}_h$ local velocity field in the rotor-fixed frame of reference

https://doi.org/10.1017/S0001924000011404 Published online by Cambridge University Press

$V(t)$ time dependent control volume
V_∞ free stream velocity
V_{loc} local velocity
$\langle V \rangle$ average velocity
V_{rot} rotational velocity
V_0 average component of the local velocity
V_{1s} Sine component of the local velocity
$\mathbf{w}_{i,j,k}$ discretised conserved variables vector
$\vec{\mathbf{w}}$ conserved variables vector
x peak-to-peak variation of the aerofoil location in the translation motion

Greek symbols

α incidence
$\overline{\alpha}$ peak-to-peak variation of the incidence
α_i modal amplitude coefficient for the *i*-th eigenmode
$\overline{\delta}_f$ peak-to-peak variation of the flap deployment
δ_f flap deployment angle
$\Delta M^2 C^*_m$ variation of the sectional pitching moment coefficient, defined in Equation (12)
$\Delta M^2 C^*_n$ variation of the sectional normal force coefficient, defined in Equation (10)
$\Delta M^2 C^*_q$ variation of the sectional torque coefficient, defined in Equation (11)
ΔZ flapping deflection
θ_{elas} elastic torsion
μ forward flight advance ratio
μ_∞ air viscosity at free stream conditions
ξ_{flap} flap damping coefficient, defined in Equation (7)
ξ_{rot} rotational damping coefficient, defined in Equation (6)
ξ_{trans} translational damping coefficient, defined in Equation (8)
ρ air density
ρ_∞ free stream air density
σ rotor solidity
ϕ_i Mass-scaled modal deformation of the *i*-th eigenmode
ϕ_0 blade shape under rotational loading
ϕ blade deformed shape
ψ blade azimuth angle
ω rotor rotational speed

1.0 INTRODUCTION

Active devices are seen as a way to improve the helicopter rotor blade performance by producing optimised aerofoil shapes for both transonic speeds on the advancing side, and low speed at high angles of attack on the retreating side. They are also seen as a means to reduce vibration and noise. During the last few years, many approaches have been tested, such as Gurney flaps[1-4] trailing-edge flaps[5-7] higher harmonic control[8,9] and active twist[10].

Many works chose a specific flight condition to apply the active device, neglecting the effect of the active device in other parts of the flight envelope. Slow descent flight conditions were favoured by a large number of researchers[3,4,10] trying to decrease the noise produced by

https://doi.org/10.1017/S0001924000011404 Published online by Cambridge University Press

blade-vortex interaction (BVI). Other works focused on one single high-speed forward flight condition[2,6,7]. As a result, benefits could be achieved at those particular conditions, but a limited number of studies looked at the effect of the flaps over the envelope of a modern helicopter rotor with composite blades.

There have been few studies with active flaps applied in the whole flight domain. Wind tunnel tests were performed by Straub *et al*[5] on the SMART blade to assess the effect of adding a trailing edge flap. That work highlighted the benefits of using flaps to lower the rotor vibration or noise on the whole flight domain, but showed little improvement in performance. Flight tests conducted by Airbus Helicopters[11] highlighted a reduction of the 4/Rev vibration levels over the whole forward flight speed range of a BK-117 helicopter equipped with trailing edge flaps. This reduction reached up to 80%, at a speed of 95kn. A study by Ravichandran *et al*[12] covered the complete flight domain of a UH-60A rotor using a trailing-edge flap. Tests were first conducted on a hovering rotor, and revealed that deploying the flaps would increase the rotor figure of merit by deforming the blade. This effect was stronger for a blade made softer in torsion. The study in forward flight at high advance ratios revealed that using 1/Rev and 2/Rev actuation sequences could improve the performance by reducing the required power by up to 5%. One high-speed condition was also chosen to test the effectiveness of flaps at reducing the levels of hub load vibrations, using a combination of 3 to 5/rev actuation. About 80% reduction in the vibratory loads was achieved. However, such high reduction in terms of vibration led to increased power requirements. With a particular actuation at 1-5/Rev, benefits could be achieved in both performance and vibration. Similar work has been performed using Gurney flaps[1] or tabs[13].

The present work considers the effect of trailing edge flaps on the whole flight domain of a modern mid-sized helicopter main rotor using computational fluid dynamics (CFD). After the CFD solver and the dMdt approach are presented, selected sections of the rotor are studied in dynamic stall conditions, and using dMdt simulations. This is followed by simulations of the rotor in hover and forward flight.

2.0 CFD METHODOLOGY

2.1 CFD solver

The helicopter multi-block (HMB2) code[14], developed at the University of Liverpool, is used as the CFD solver for the present work, for both 2D and 3D simulations. It solves the Navier-Stokes equations in integral form using the arbitrary Lagrangian Eulerian (ALE) formulation for time-dependent domains with moving boundaries:

$$\frac{\mathrm{d}}{\mathrm{d}t}\int_{V(t)} \vec{\mathbf{w}}\,\mathrm{d}V + \int_{\partial V(t)} \left(\vec{F}_i\left(\vec{\mathbf{w}}\right) - \vec{F}_v\left(\vec{\mathbf{w}}\right)\right)\vec{n}\,\mathrm{d}S = \vec{S} \qquad \ldots (1)$$

where $V(t)$ is the time dependent control volume, $\partial V(t)$ its boundary, $\vec{\mathbf{w}}$ is the vector of conserved variables $[\rho, \rho u, \rho v, \rho w, \rho E]^T$. $\vec{F}_i$ and $\vec{F}_v$ are the inviscid and viscous fluxes, including the effects of the time dependent domain. For forward flying rotor simulations, a moving grid approach is used and the source term is set to zero.

The Navier-Stokes equations are discretised using a cell-centred finite volume approach on a multi-block grid, leading to the following:

$$\frac{\partial}{\partial t}\left(\mathbf{w}_{i,j,k} V_{i,j,k}\right) = -\mathbf{R}_{i,j,k}\left(\mathbf{w}_{i,j,k}\right) \qquad \ldots (2)$$

https://doi.org/10.1017/S0001924000011404 Published online by Cambridge University Press

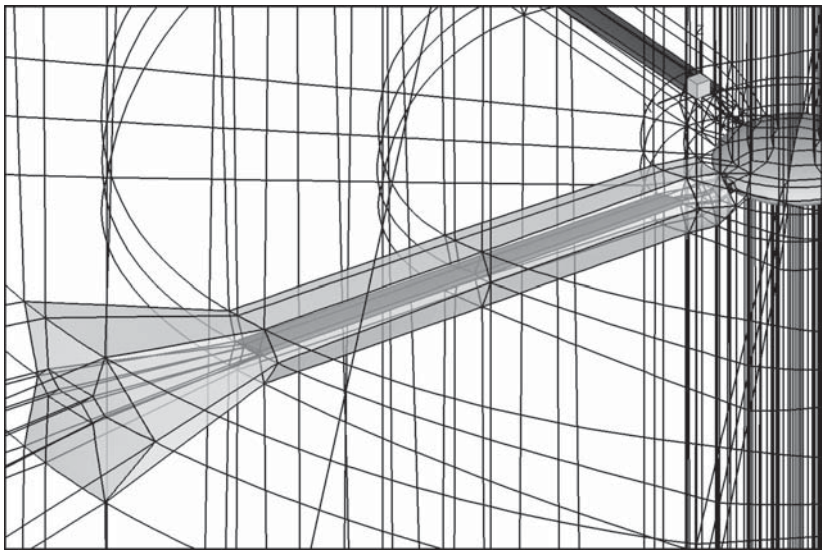

Figure 1. Rigid blocks (light grey) used for rotor trimming in HMB, for forward flight configurations. The blade is shown in dark grey and the hub in light grey.

where **w** represents the cell variables and **R** the flow residuals. i, j and k are the cell indices and $V_{i,j,k}$ is the cell volume. Osher's[15] upwind scheme is used to discretise the convective terms and monotonic upstream-centered scheme for conservation laws (MUSCL) variable interpolation[16] is used to provide third order accuracy. The Van Albada limiter[17] is used to prevent oscillations near steep gradients. Menter's k-ω SST turbulence model [18] was used for all simulations.

Temporal integration is performed using an implicit dual-time step method. The linearised system is solved using the generalised conjugate gradient method with a block incomplete lower-upper (BILU) pre-conditioner [19].

Multi-block structured grids are used with HMB2, and are generated using ICEM-Hexa of ANSYS[20]. The multi-block topology allows for an easy sharing of the calculation load for parallel computing. For rotor flows, the typical multi-block topology of the University of Liverpool, as described in Ref. 21, was used. It is based on a C-mesh topology around the blade that is included in a larger H structure which fills up the rest of the computational domain. The block boundaries for a forward flying ONERA 7A rotor are shown in black in Fig. 1.

The mesh deformation method used for the flap motion is described by Steijl *et al*[22]. The mesh on the flap surface is rotated to the new flap angle around the hinge, and linear blending is applied to the nodes near the flap spanwise ends, to remove strong mesh discontinuities.

In forward flight, when a rigid blade model is not considered, the blade deformation due to the structural properties is prescribed. The deformation was based on in-flight measurements, and a modal analysis of the blade. The blade shape was then described as:

$$\phi = \phi_0 + \sum_{i=1}^{n_m} \alpha_i \phi_i \qquad \ldots (3)$$

where ϕ is the blade shape, ϕ_0 the shape of the blade undeformed and ϕ_i is the ith eigenmode of the blade. The amplitude coefficients α_i were obtained from in-flight measurements.

https://doi.org/10.1017/S0001924000011404 Published online by Cambridge University Press

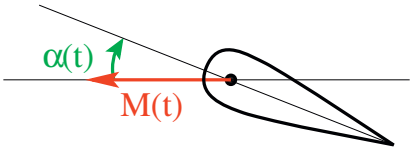

Figure 2. Aerofoil motion in a dMdt simulation.

The mesh deformation methods of HMB2 first deform the blade surface using the constant volume tetrahedron (CVT) method, then obtain the updated block vertex positions via spring analogy (SAM) and finally generate the full mesh via transfinite interpolation (TFI). The method is described in detail in Ref. 23. The TFI first interpolates the block edges and faces from the new vertex position and then interpolates the full mesh from the surfaces. This method uses the properties of multi-block meshes and maintains efficiency as the number of blocks increases, particularly in the spanwise blade direction. This approach is not reported elsewhere in the literature since most authors deform the complete mesh using the mode shapes. The proposed method provides more flexibility and allows for complex multi-block topologies to be used. In addition, it gives more control over the distribution of mesh deformation in the computational domain.

The constant volume tetrahedron (CVT) method developed by Goura[24] allows for quick deformation calculations. This method projects each fluid node to the nearest structural triangular element and moves it linearly with the element. The volume of the pyramid made of the triangular structural element and the fluid mesh point is kept constant. While the CVT is not strictly following the global conservation law, it was demonstrated through numerical simulations that the differences are negligible[24].

The spring analogy[25] consists of adding springs on each block face and diagonal of the mesh. The springs along the sides of the surfaces tend to avoid large compression or dilatation of the block surfaces and the ones on the diagonals tend to limit skewness, which is critical in some parts of the mesh like the tip of the blade where the cells are usually skewed. The strengths of the springs are set as the inverse of their length and the springs in contact with the blade are usually made stiffer by a coefficient arbitrarily set to 50 to make the blocks close to the blade surface extremely rigid. This is described in detail in Dehaeze and Barakos[23].

The transfinite interpolation (TFI)[26] method is finally used to regenerate the mesh in each individual block. This method is quick and allows for the mesh deformation time to be low, which is required in rotorcraft simulations due to the need to deform the mesh at each time steps.

2.2 dMdt simulations

dMdt simulations consider a translating and pitching aerofoil, aiming to approximate the conditions experienced by a rotor section without the cost of a full 3D rotor simulation. Such simulations can be used to assess the aerodynamic models employed in blade element methods, which usually obtain the sectional lift and drag based on aerofoil polars, corrected for the pitching motion. In dMdt simulations, changes in incidence are obtained by modifying the pitch angle, while changes in velocity are obtained by modifying the translational mesh speed, as shown in Fig. 2. Unlike blade element models, which usually only account for the incidence, Mach number, Reynolds number, and have a model for the influence of the variation of the incidence, dMdt simulations also take into account the unsteady variation of the Mach and Reynolds numbers.

To achieve the required incidence and velocity, the mesh is translated and rotated. Starting with

https://doi.org/10.1017/S0001924000011404 Published online by Cambridge University Press

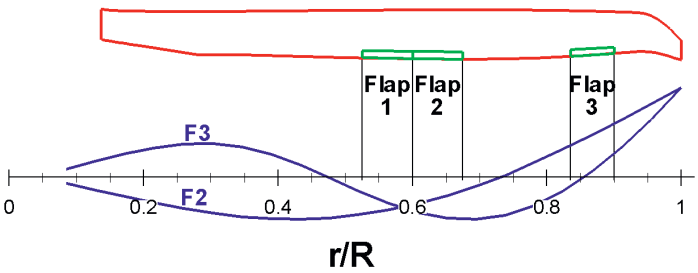

Figure 3. Location of the flaps on the blade compared to the second and third flapping mode shapes.

a mesh containing an aerofoil at zero incidence, the aerofoil is rotated around the quarter-chord to reach the required incidence, and then translated along the *X*-axis to adjust the velocity. The far field velocity is always applied along the positive *X*-axis and is defined as the local rotational speed $V_{rot} = \frac{r}{R} V_{tip}$. The aerofoil position along the *X*-axis is then defined as:

$$x = -\frac{V_\infty}{\omega} \mathrm{Cos}\psi \quad . \qquad \ldots (4)$$

The aerofoil translation will then create the required changes in sectional chordwise velocity. The local velocity, matching a real forward flight case is then obtained by:

$$V_{loc}(\psi) = \frac{r}{R} V_{tip} + V_\infty \mathrm{Sin}(\psi) \quad . \qquad \ldots (5)$$

The flow field is computed at every azimuth using a time-marching approach. In the present work, five cycles were enough to reach convergence of the loads. With the mesh size used here (around 150,000 nodes), the simulation took around 40 hours of a single core on an Intel Xeon CPU operating at 3·5GHz.

3.0 RESULTS AND DISCUSSION

A five-bladed main rotor, representative of a modern design was used in this work. The blade planform can be seen in Fig. 3, and had a nominal twist of 11°/*R*. Three flaps were added to the blade, located near the antinodes of the second and third flapping modes. The blade uses three modern rotorcraft aerofoil sections along the span.

3.1 2D Aerofoil study

3.1.1 Pitching aerofoils

A first test was performed on pitching aerofoils. Two sections of the main rotor blade were selected: one centred at r/R = 0·6 and another one at r/R = 0·8. All test cases were run at M_∞ = 0·3 and $Re_\infty = 4{\cdot}2 \times 10^6$. Eight conditions were chosen for the pitching simulations and are shown in Table 1. At all conditions, three flap positions were tested: δ_f = 0 °, δ_f = –2·5° and δ_f = 4·5°. A moving

https://doi.org/10.1017/S0001924000011404 Published online by Cambridge University Press

Table 1
Conditions for the pitching aerofoil case

Sections	M_∞	Re_∞	$k = \omega c/2V_\infty$	α(degrees)	δ_f(degrees)
Inboard	0·3	$4{\cdot}2 \times 10^6$	0·8	10 + 5 Sin(ψ)	0, –2·5, 4·5, 3 + 3 Sin (ψ)
Inboard	0·3	$4{\cdot}2 \times 10^6$	0·8	10 + 10 Sin(ψ)	0, –2·5, 4·5, 3 + 3 Sin (ψ)
Inboard	0·3	$4{\cdot}2 \times 10^6$	0·8	14 + 5 Sin(ψ)	0, –2·5, 4·5, 3 + 3 Sin (ψ)
Inboard	0·3	$4{\cdot}2 \times 10^6$	0·8	14 + 14 Sin(ψ)	0, –2·5, 4·5, 3 + 3 Sin (ψ)
Inboard	0·3	$4{\cdot}2 \times 10^6$	0·12	10 + 5 Sin(ψ)	0, –2·5, 4·5
Inboard	0·3	$4{\cdot}2 \times 10^6$	0·12	10 + 10 Sin(ψ)	0, –2·5, 4·5
Inboard	0·3	$4{\cdot}2 \times 10^6$	0·12	14 + 5 Sin(ψ)	0, –2·5, 4·5
Inboard	0·3	$4{\cdot}2 \times 10^6$	0·12	14 + 14 Sin(ψ)	0, –2·5, 4·5
Outboard	0·3	$4{\cdot}2 \times 10^6$	0·08	10 + 5 Sin(ψ)	0, –2·5, 4·5
Outboard	0·3	$4{\cdot}2 \times 10^6$	0·08	10 + 10 Sin(ψ)	0, –2·5, 4·5
Outboard	0·3	$4{\cdot}2 \times 10^6$	0·08	14 + 5 Sin(ψ)	0, –2·5, 4·5
Outboard	0·3	$4{\cdot}2 \times 10^6$	0·08	14 + 14 Sin(ψ)	0, –2·5, 4·5
Outboard	0·3	$4{\cdot}2 \times 10^6$	0·12	10 + 5 Sin(ψ)	0, –2·5, 4·5
Outboard	0·3	$4{\cdot}2 \times 10^6$	0·12	10 + 10 Sin(ψ)	0, –2·5, 4·5
Outboard	0·3	$4{\cdot}2 \times 10^6$	0·12	14 + 5 Sin(ψ)	0, –2·5, 4·5
Outboard	0·3	$4{\cdot}2 \times 10^6$	0·12	14 + 15 Sin(ψ)	0, –2·5, 4·5

flap was also tested on the inboard section, using an actuation of $\delta_f = 3 - 3\mathrm{Sin}(\psi)$.

The aerodynamic damping coefficient of the pitching motion during a cycle, defined as:

$$\xi_{rot} = -\frac{1}{\frac{1}{2}\rho_\infty < V >^2 c^3 \pi \bar{\alpha}^2} \int_{cycle} M_{pitch} \mathrm{d}\alpha \qquad \ldots (6)$$

was extracted and is shown in Fig. 4(a) for the inboard section and 4(b) for the outboard section. Only one case led to a negative damping coefficient, corresponding to the inboard section with $\alpha = 14 - 5\,\mathrm{Sin}(\psi)°$, and a flap position of $\delta_f = -2{\cdot}5°$. All other cases led to positive damping coefficients, highlighting the stability of the aerofoil in pitching motions.

For the cases where the flap was actuated, the damping coefficient of the flap rotation around his hinge, defined as:

$$\xi_{flap} = -\frac{1}{\frac{1}{2}\rho_\infty < V >^2 c^3 \pi \bar{\alpha}^2} \int_{cycle} M_H \mathrm{d}\delta_f \qquad \ldots (7)$$

was extracted and is shown in Fig. 4(c). Negative values highlight flap instabilities. For the second case where the negative damping coefficient was close to $\alpha = 10 - 10\,\mathrm{Sin}(\psi)°$ and could easily be compensated by the structural and mechanical losses, in the fourth case where $\alpha = 14 - 14\,\mathrm{Sin}(\psi)°$, the damping was clearly negative.

3.1.2 dMdt simulations

Eight dMdt simulations were carried out, following the approach described in Section 2.2. Their conditions are shown in Table 2. These conditions are representative of sections at $r/R = 0{\cdot}6$ (Cases

https://doi.org/10.1017/S0001924000011404 Published online by Cambridge University Press

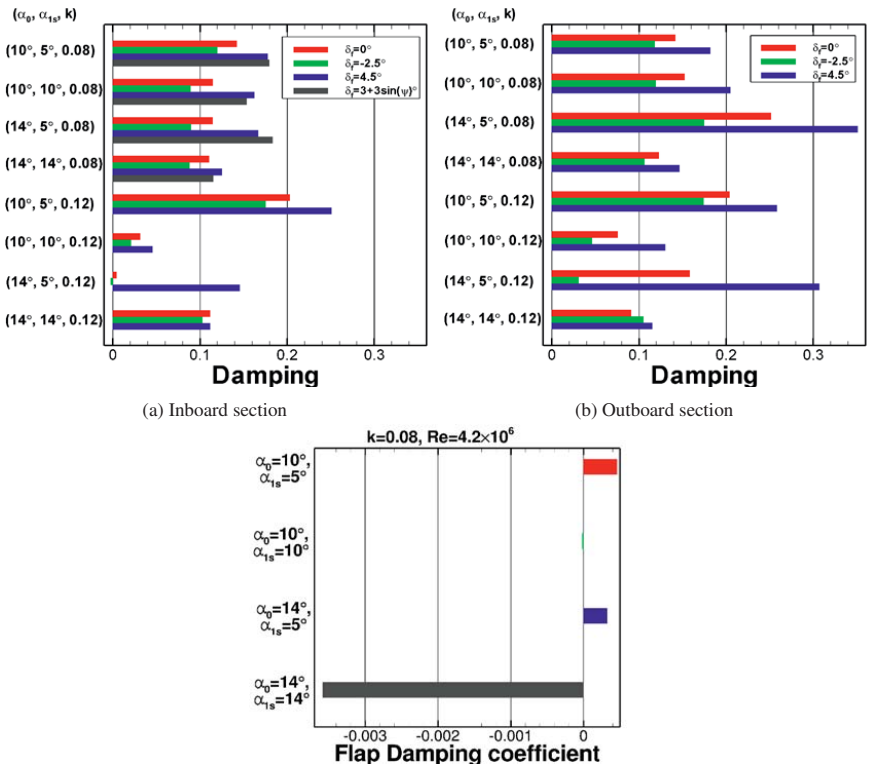

(a) Inboard section

(b) Outboard section

(c) Flap damping

Figure 4. Aerodynamic damping coefficient for pitching inboard and outboard sections, and aerodynamic flap damping when they are actuated.

Table 2
Conditions for the dMdt cases

Case	Section	M_∞	Re_∞	α(degrees)	δ_f(degrees)
1	Inboard	0·378 + 0·24 Sin(ψ)	5·418 × 10^6	7 – 5 Sin(ψ)	0
2	Inboard	0·378 + 0·24 Sin(ψ)	5·418 × 10^6	7 – 5 Sin(ψ)	–2·5
3	Inboard	0·378 + 0·24 Sin(ψ)	5·418 × 10^6	7 – 5 Sin(ψ)	4·5
4	Inboard	0·378 + 0·24 Sin(ψ)	5·418 × 10^6	7 – 5 Sin(ψ)	1 – 3·5 Sin (ψ)
5	Outboard	0·5 + 0·24 Sin(ψ)	7·0 × 10^6	5 – 5 Sin(ψ)	0
6	Outboard	0·5 + 0·24 Sin(ψ)	7·0 × 10^6	5 – 5 Sin(ψ)	–2·5
7	Outboard	0·5 + 0·24 Sin(ψ)	7·0 × 10^6	5 – 5 Sin(ψ)	4·5
8	Outboard	0·5 + 0·24 Sin(ψ)	7·0 × 10^6	5 – 5 Sin(ψ)	1 – 3·5 Sin (ψ)

1-4) and at $r/R = 0{\cdot}8$ (Cases 5-8). Figure 5 shows snapshots of the flow field at various azimuths: the contours show the pressure coefficient. The wake velocity in the aerofoil frame of reference was also extracted at two stations downstream from the aerofoil. The pressure coefficients C_P were extracted and scaled using the local velocity: $C_P = \frac{P-P_\infty}{\frac{1}{2}\rho_\infty V_{loc}^2}$, with

https://doi.org/10.1017/S0001924000011404 Published online by Cambridge University Press

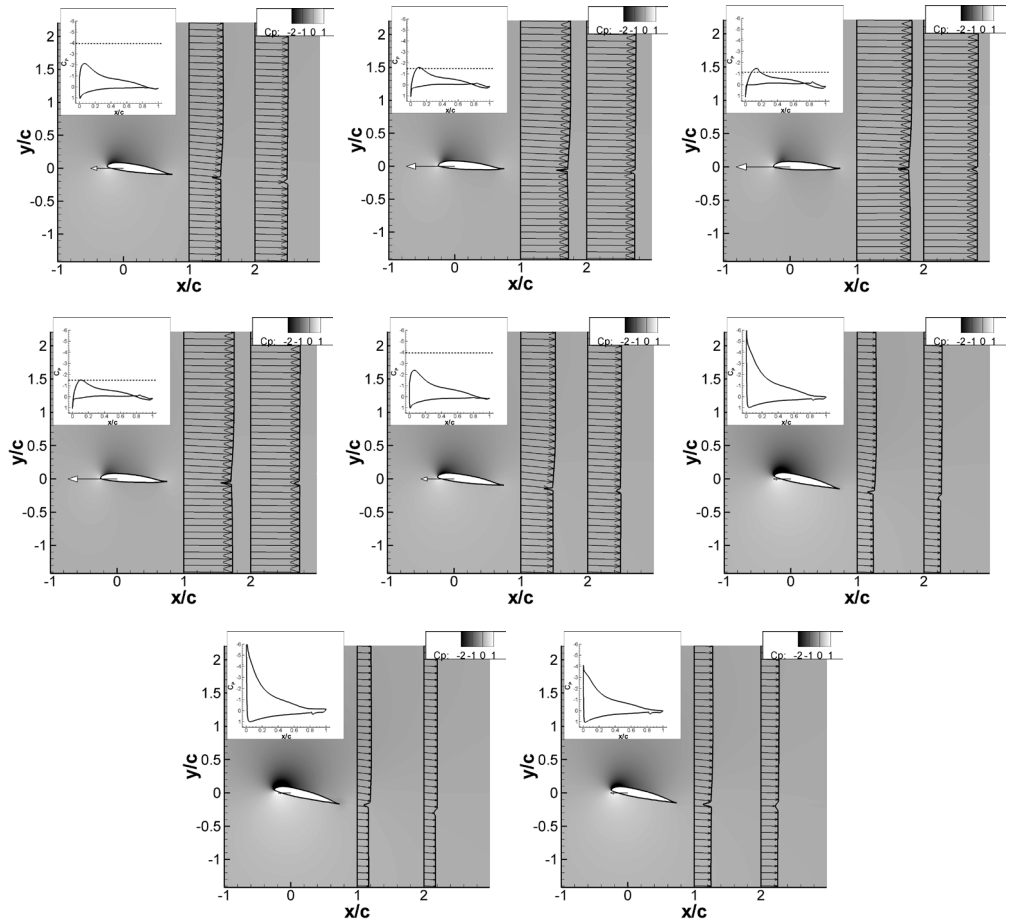

Figure 5. Pressure coefficient around the inboard section and velocity distribution (using the aerofoil frame of reference) along two stations in the wake, Case 4. In the aerofoil pressure coefficient plots, the critical pressure coefficient is shown with a dashed line.

$V_{loc}(\psi) = V_0 + V_{1s}\,\mathrm{Sin}(\psi)$. A shock can clearly be seen on the advancing side at $\psi = 90°$, while high suction appears on the retreating side at $\psi = 270°$.

The lift, drag and moment coefficients were extracted, and shown in Fig. 6 for Cases 1-4, and in Fig. 7 for Cases 5-8. The most noticeable feature is the negative drag coefficient on the retreating side when the flap is deployed, appearing at both sections, and more pronounced on the inboard section. This comes from the rapid increase in pitch and deceleration of the aerofoil, as well as the influence of the modified wake compared to static aerofoils, that made the current measure of the incidence, relative to the flow direction at the far field, non representative of the actual local incidence the aerofoil sees.

Symbols were also added in the lift, drag and moment coefficients plots, showing the force and moment predictions if a steady flow is used, by extracting the lift, drag and moment coefficients from static polars at similar conditions, when available. For Cases 1-4, while the comparison was fair on the advancing side, the predictions at the conditions of the retreating side were off. For Cases 5-8, the coefficients from the dMdt and the static simulations did not match. This highlights

https://doi.org/10.1017/S0001924000011404 Published online by Cambridge University Press

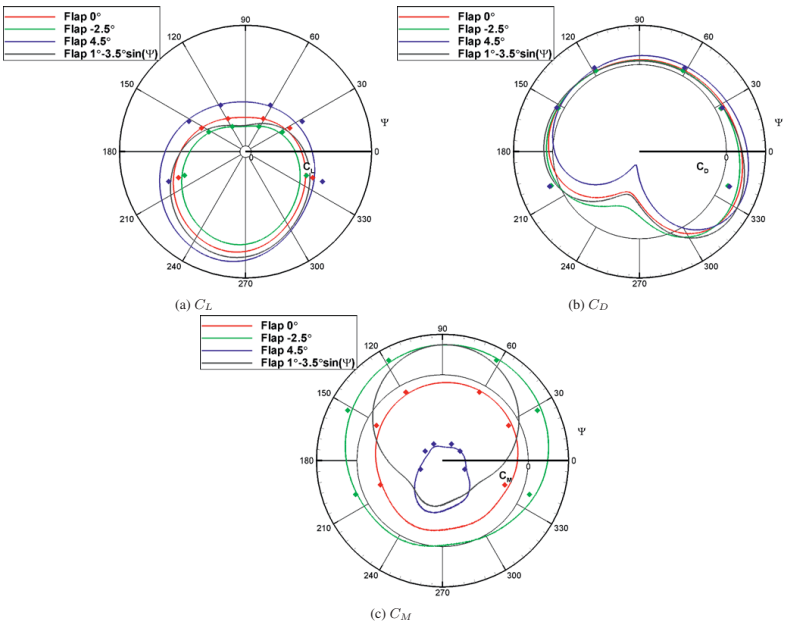

(a) C_L (b) C_D

(c) C_M

Figure 6. Lift, drag and moment coefficients as a function of the azimuth for a dMdt simulation, Cases 1-4. The symbols show the force and moment coefficients obtained when using static simulations at similar conditions.

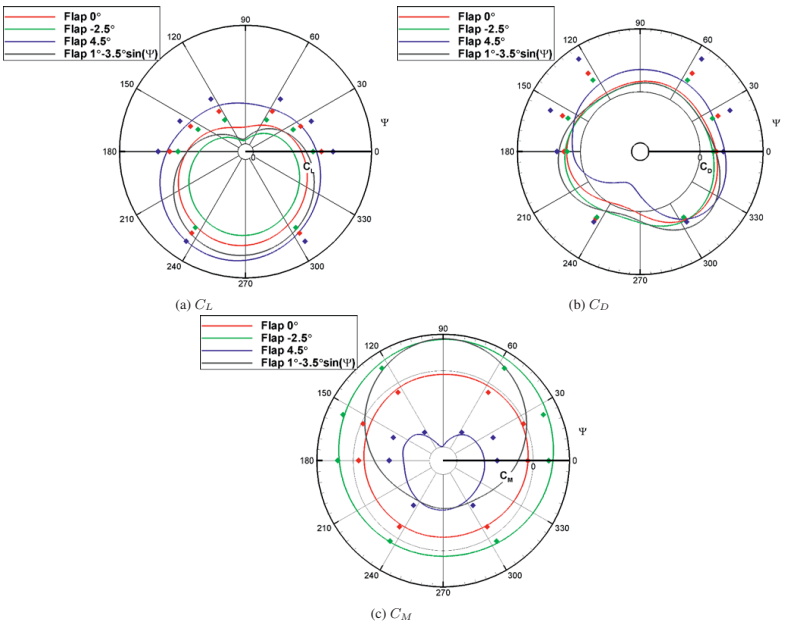

(a) C_L (b) C_D

(c) C_M

Figure 7. Lift, drag and moment coefficients as a function of the azimuth for a dMd*t* simulation, Cases 5-8. The symbols show the force and moment coefficients obtained when using static simulations at similar conditions.

https://doi.org/10.1017/S0001924000011404 Published online by Cambridge University Press

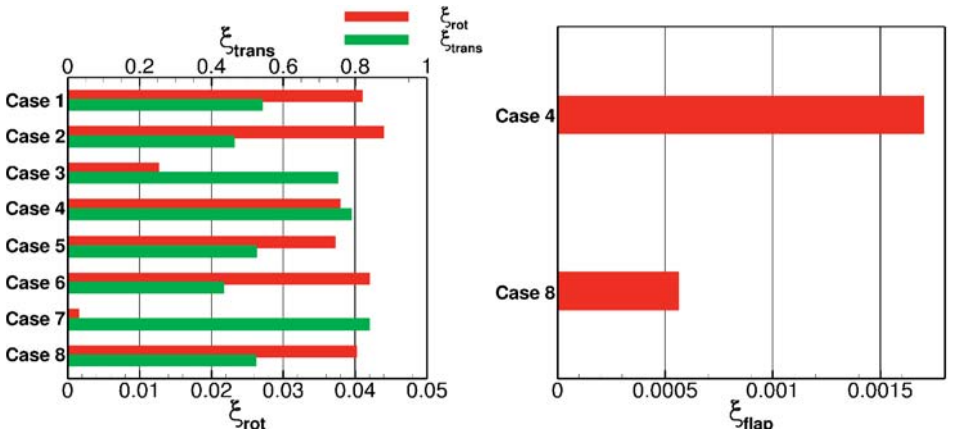

Figure 8. Damping coefficient of the aerofoil in translation and pitching, and damping coefficient of the flap deployment when available.

the importance in taking into account the dynamic effects due to the changes in pitch and speed in blade element models.

Again, the aerodynamic damping coefficients in translation and pitching were computed. The aerodynamic damping coefficient in pitching was defined in Equation (6), and the aerodynamic damping coefficients in translation is defined as follows:

$$\xi_{trans} = \frac{1}{\frac{1}{2}\rho_{\infty} < V >^2 c^2 \pi \bar{x}^2} \int_{cycle} F_{drag} \mathrm{d}x \qquad \ldots (8)$$

They are shown for each case in Fig. 8. The translational variations always proved stable, with high damping coefficients. Pitching damping coefficients from all cases also showed a positive damping, but when the cycle was simulated with a fully deployed flap (Cases 3 and 7), the damping coefficient was lower, becoming very small in the case of the outboard section (Case 7). This goes against what was observed for pitching aerofoils (Figs 4(a) and 4(b)), where deploying the flap increased the damping coefficient.

3.2 Main rotor in hover

The main rotor, previously described, was equipped with flaps, as shown in Fig. 3. The flaps were located near the anti-nodes of the second and third flapping modes, to allow for vibration control. In hover, all flaps were synchronised and were tested at two deployed positions: $\delta_f = -2{\cdot}5°$ and $\delta_f = 4{\cdot}5°$. Three collective settings were tested. The evolution of the figure of merit with the thrust coefficient is shown in Fig. 9. The figure of merit, the ratio of induced power to total power, is an indicator of the rotor performance in hover, and is defined as:

$$FM = \frac{C_T^{\frac{3}{2}}}{2C_Q} \qquad \ldots (9)$$

https://doi.org/10.1017/S0001924000011404 Published online by Cambridge University Press

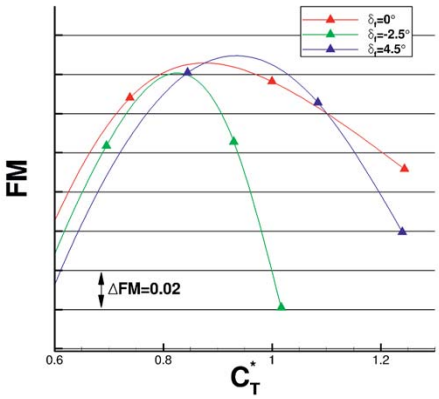

Figure 9. Changes in the figure of merit with the flap deployment in hover.

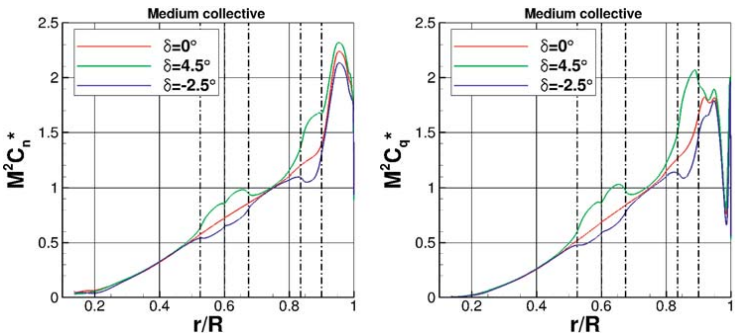

Mach-scaled normal force coefficient Mach-scaled torque coefficient

Figure 10. Distribution of the Mach-scaled normal force and torque coefficients predictions, with and without flap deployment, for a hovering main rotor blade at a medium collective level. The coefficients were scaled with their value at r/R = 0·75 in the case without flap.

Since the blade is based on a commercial design, the actual value of the figure of merit could not be shown, only the differences are presented. Three points were simulated for each flap setting, and trends were interpolated, as shown on the graph. Deploying the flaps up did not bring any improvement; however, setting the flaps at δ_f = 4·5° improved the figure of merit for a limited range of high thrust coefficients.

The distributions of the sectional thrust and torque were extracted for the medium collective case, and are shown in Fig. 10. The sectional thrust and torque were scaled using their value at r/R = 0·75 in the case without flaps. The location of the flaps is shown using dash-dotted lines. The effect of the inboard flaps on the loading proved to be limited to the flap area and its close surroundings. On the other hand, the tip flap also modified the blade loading outboard of the flap all the way to the tip. This alteration of the loading had an influence on the induced power, which might not be beneficial and could explain the limited benefit in performance when deploying the flaps in hover.

https://doi.org/10.1017/S0001924000011404 Published online by Cambridge University Press

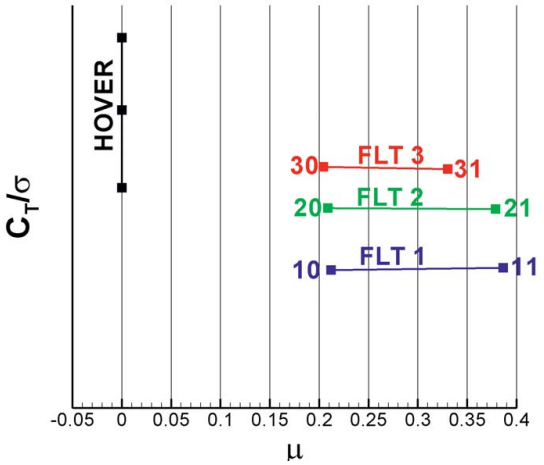

Figure 11. Flight conditions for the forward flight simulations.
The hover simulations performed without flaps are added for reference.

3.3 Main rotor in forward flight

The same rotor was simulated in forward flight to assess the effect of the flaps over the whole flight envelope. In total, six cruise level flights were simulated, at low and high speeds at three different thrust settings. A summary of the flight conditions is shown in Fig. 11. For these simulations, the blade was considered rigid, and the rotor was computed without flap actuation, or with all flaps actuated with $\delta_f = 3 - 3\ \mathrm{Sin}(\psi)°$. The main goal of the flap actuation was to alleviate the stall on the retreating side and improve the rotor performance.

For each flight, the sectional thrust, torque and pitching moments were calculated. Their values for the cases without flap were substracted from the values with flaps, and the result was divided by the maximum absolute value without flap:

$$\Delta \mathrm{M}^2 C_n^* = \frac{\mathrm{M}^2 C_{n,with\ flap} - \mathrm{M}^2 C_{n,without\ flap}}{\max(|\,\mathrm{M}^2 C_{n,without\ flap}\,|)} \quad \ldots (10)$$

$$\Delta \mathrm{M}^2 C_q^* = \frac{\mathrm{M}^2 C_{q,with\ flap} - \mathrm{M}^2 C_{q,without\ flap}}{\max(|\,\mathrm{M}^2 C_{q,without\ flap}\,|)} \quad \ldots (11)$$

$$\Delta \mathrm{M}^2 C_m^* = \frac{\mathrm{M}^2 C_{m,with\ flap} - \mathrm{M}^2 C_{m,without\ flap}}{\max(|\,\mathrm{M}^2 C_{m,without\ flap}\,|)} \quad \ldots (12)$$

The Mach-scaled sectional forces and moments, as well as resulting variation ratios, are shown for each flight in Figs 12-17.

In most flights, a strong effect on the pitching moment was seen at the location of the flaps, with the pitching moment amplitudes increasing by 12% or more. At high thrust coefficient, the flaps delayed the effect of the stall on the retreating side. This can be seen in Figs 12 and 13, where the stall on the retreating side is clearly visible due to the drop in moments shown in Figs 12(e) and

https://doi.org/10.1017/S0001924000011404 Published online by Cambridge University Press

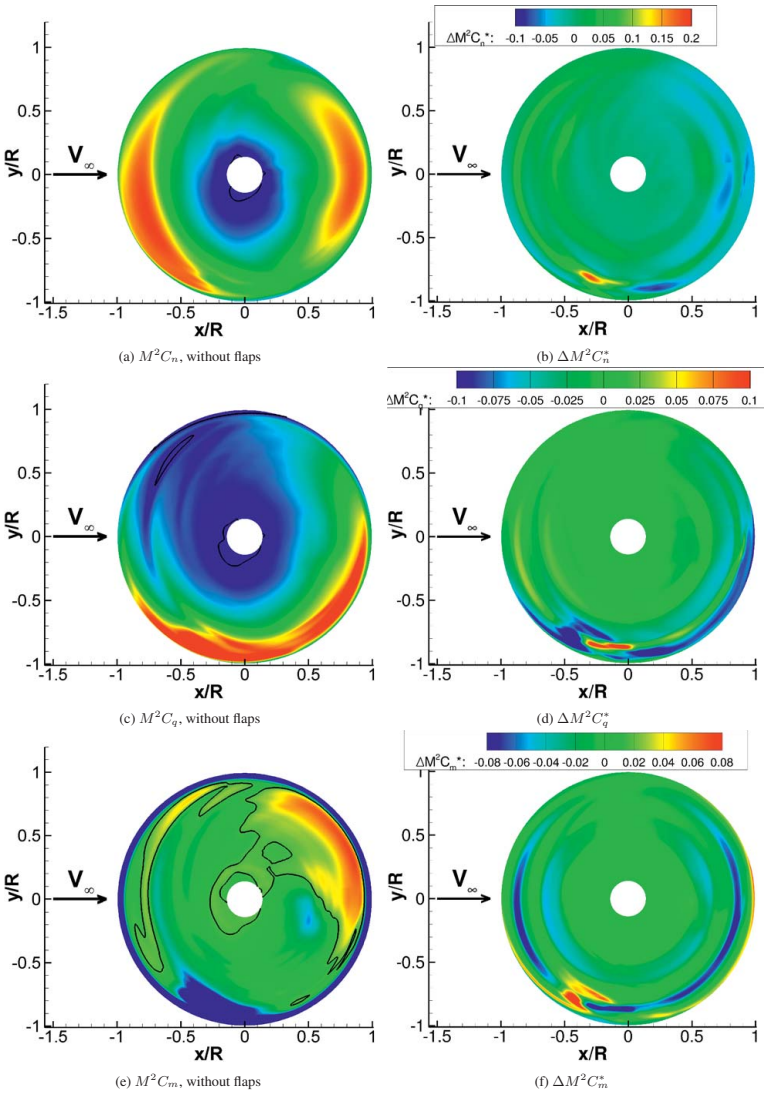

(a) M^2C_n, without flaps (b) $\Delta M^2C_n^*$

(c) M^2C_q, without flaps (d) $\Delta M^2C_q^*$

(e) M^2C_m, without flaps (f) $\Delta M^2C_m^*$

Figure 12. Mach-scaled normal force, torque and moment coefficient predictions for Flight 3-30. In the plots without flaps, a thick black lines indicates a value of 0.

13(e). It can be seen that the stall is delayed in Figs 12(f) and 13(f), where the high positive values of $\Delta M^2C_m^*$ at the stall location indicate that the pitching moment did not drop as early. At medium thrust, the main effect of the flaps at low speed was to modify the blade-vortex interaction in the second quarter of the disk as seen in Fig. 14, where high variations of the M^2C_n and M^2C_m coefficients can be seen, but at high speed, the flap mainly affected the thrust on the advancing side, and the stall on the retreating side (Fig. 15). At low thrust, the main effect of the flaps was to locally increase the thrust and the torque at the location of the flaps, as shown in Figs 16-17. It also had an effect on the blade-vortex interactions at the front of the disk. It was also seen that, at all conditions, the use of

https://doi.org/10.1017/S0001924000011404 Published online by Cambridge University Press

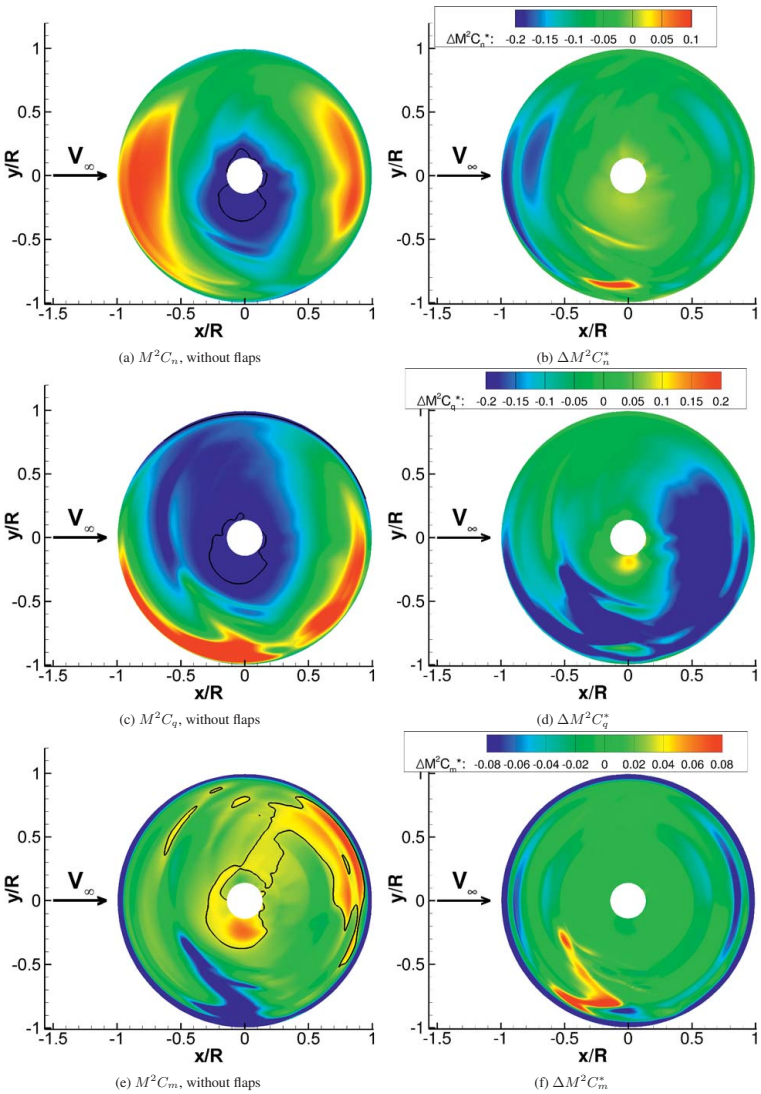

Figure 13. Mach-scaled normal force, torque and moment coefficient predictions for Flight 3-31. In the plots without flaps, thick black lines indicate a value of 0.

flaps on the blade could largely increase the levels of sectional pitching moment where the flaps are located, which could result in higher control loads.

A comparison of the resulting thrust and torque for the cases with and without flaps is shown in Fig. 18. While the obtained rotor thrust in the cases with and without flaps were not always matching due to the applied trim state, it can be seen that in some cases, some benefit can be obtained from the flaps. At high thrust and low speed, for a similar thrust, the flaps allowed for a reduction of 5% of the torque. At high thrust and high speed though, the thrust was kept similar but the required torque was largely increased. At medium thrust and low speed, the thrust was

https://doi.org/10.1017/S0001924000011404 Published online by Cambridge University Press

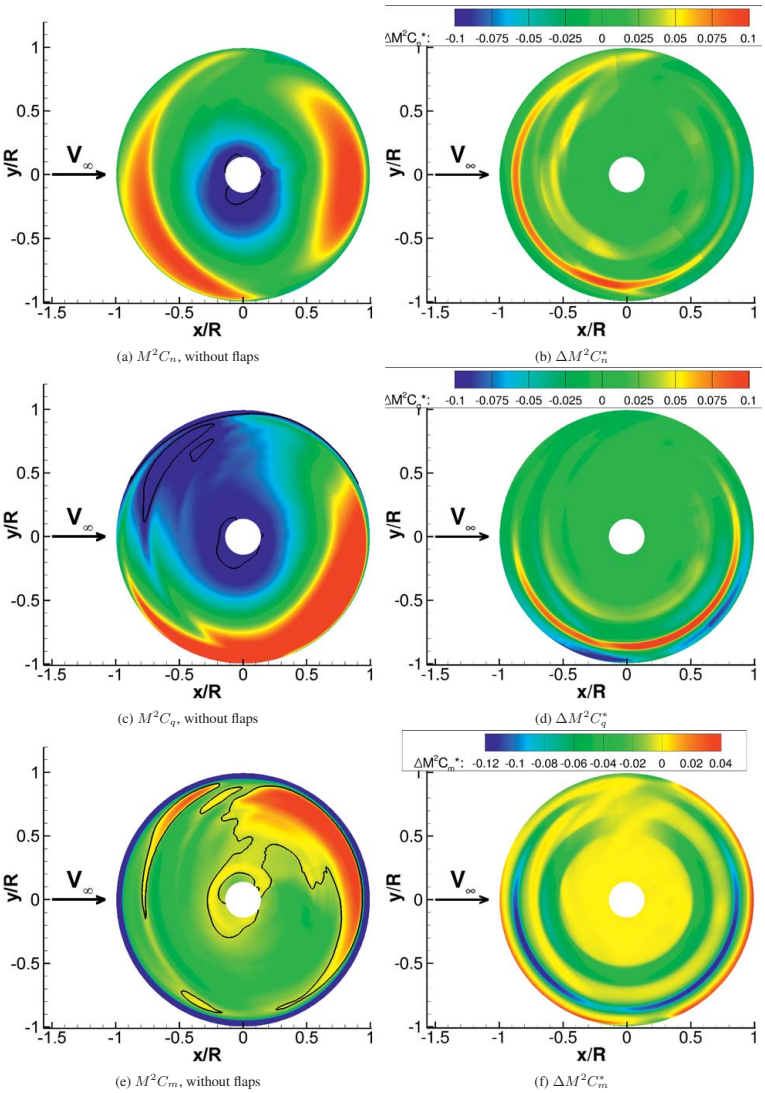

Figure 14. Mach-scaled normal force, torque and moment coefficient predictions for Flight 2-20. In the plots without flaps, thick black lines indicate a value of 0.

increased by 2·5% by actuating the flaps while the torque was slightly reduced. At low thrust, no noticeable gain was achieved. It can therefore be inferred that the benefits of flaps are limited to the high thrust or high speed, where the blade on the retreating side stalls and the flaps provided some alleviation. If the stall is too deep, however, the flaps cannot reduce its effect and the resulting required power is similar or even higher than the original requirement.

Using the conditions from Flight 2-21 (medium thrust, high speed, see Fig. 11), prescribed blade deformations were also applied to the rotor, based on in-flight measurements. The applied deformations are shown in Fig. 19. The same deformation had to be applied to the blades with and

https://doi.org/10.1017/S0001924000011404 Published online by Cambridge University Press

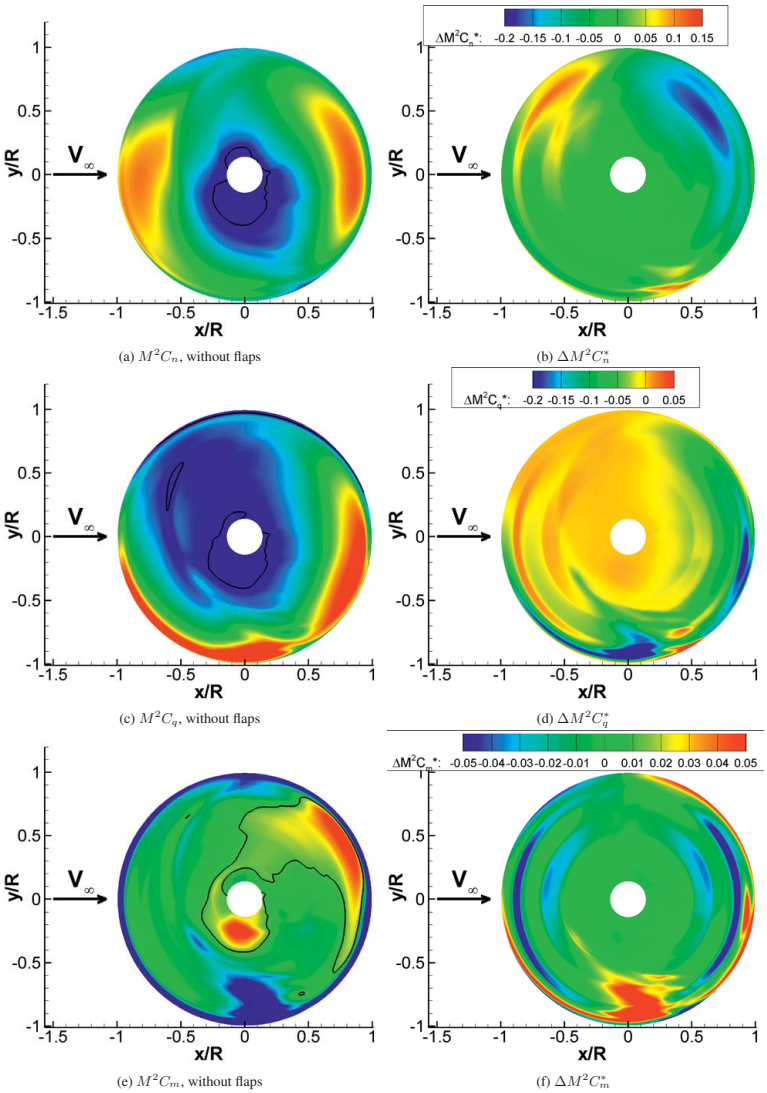

(a) M^2C_n, without flaps (b) $\Delta M^2C_n^*$

(c) M^2C_q, without flaps (d) $\Delta M^2C_q^*$

(e) M^2C_m, without flaps (f) $\Delta M^2C_m^*$

Figure 15. Mach-scaled normal force, torque and moment coefficient predictions for Flight 2-21. In the plots without flaps, thick black lines indicate a value of 0.

without flaps actuated, due to a lack of data for cases with flaps. The new differences in sectional coefficient between the cases with and without actuated flaps are shown in Fig. 20. The sectional loads for the case without flaps are also shown, using the same scale as the one used in Fig. 15. The most noticeable change is the much lower sectional lift on the advancing side seen in Fig. 19. It can be seen that the actual difference in aerodynamic loads is very similar to the rigid case shown in Fig. 15, meaning that the effect of the blade deformation on the sectional thrust and torque for both cases was similar.

https://doi.org/10.1017/S0001924000011404 Published online by Cambridge University Press

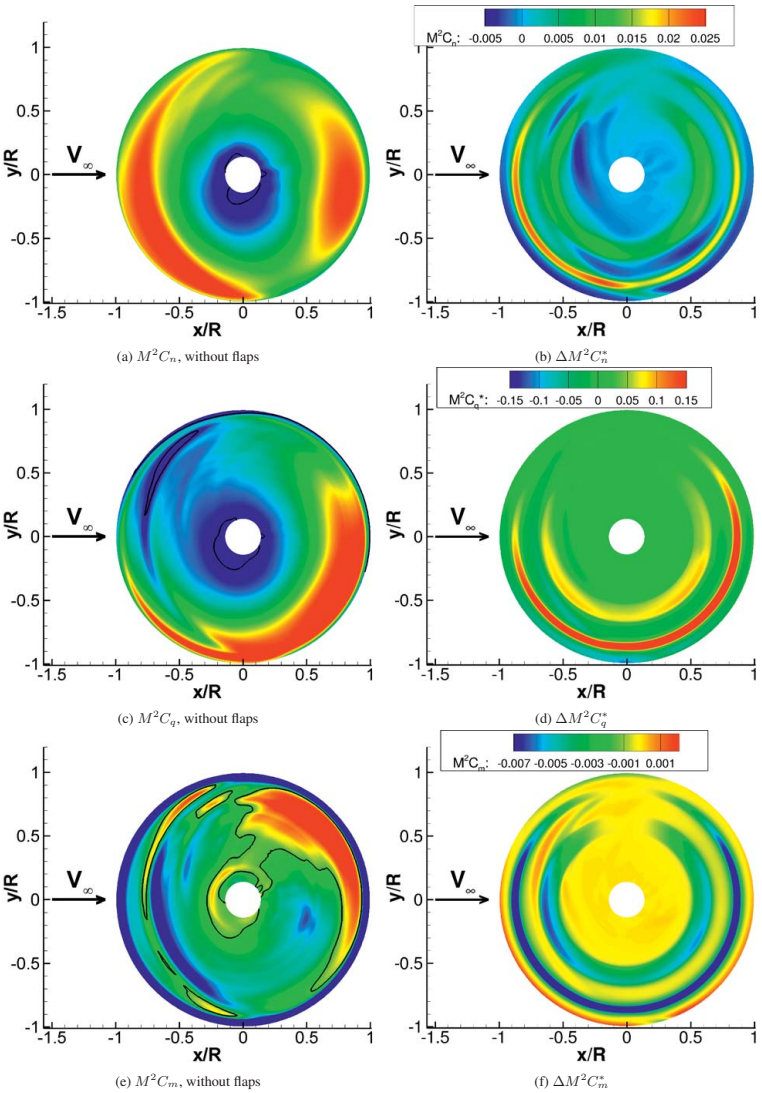

(a) M^2C_n, without flaps (b) $\Delta M^2C_n^*$

(c) M^2C_q, without flaps (d) $\Delta M^2C_q^*$

(e) M^2C_m, without flaps (f) $\Delta M^2C_m^*$

Figure 16. Mach-scaled normal force, torque and moment coefficient predictions for Flight 1-10. In the plots without flaps, thick black lines indicate a value of 0.

4.0 SUMMARY AND CONCLUSIONS

A CFD analysis of flapped rotors has been carried out, showing various ways to assess the effect of flaps on a helicopter main rotor. On a selected main rotor designed for a medium-sized helicopter, analyses ranging from 2D pitching aerofoils to full simulations of a forward flying rotor were carried out.

The 2D analyses using the dMd*t* approach highlighted the need to take into account the dynamic

https://doi.org/10.1017/S0001924000011404 Published online by Cambridge University Press

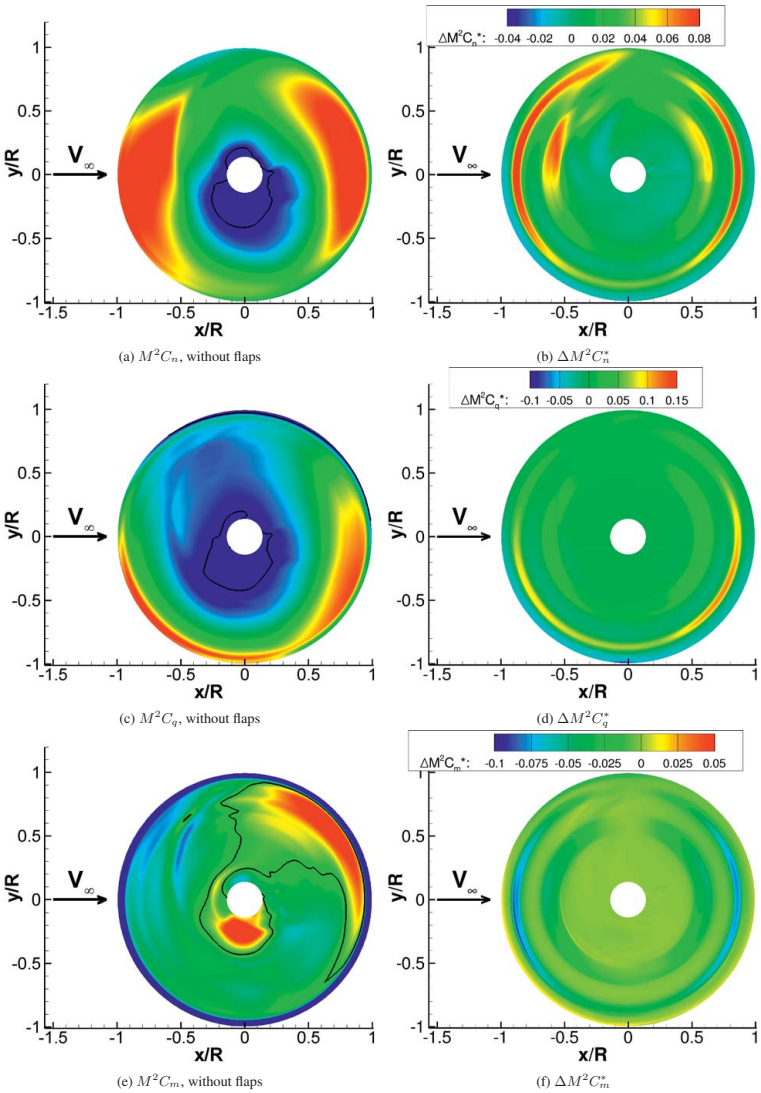

(a) M^2C_n, without flaps (b) $\Delta M^2C_n^*$

(c) M^2C_q, without flaps (d) $\Delta M^2C_q^*$

(e) M^2C_m, without flaps (f) $\Delta M^2C_m^*$

Figure 17. Mach-scaled normal force, torque and moment coefficient predictions for Flight 1-11. In the plots without flaps, thick black lines indicate a value of 0.

effects when modelling the rotor using blade element theory. The dMd*t* also proved quick to compute, and allowed to have a first estimate of the flap stability, without using expensive CFD simulations of the full rotor in forward flight.

A study of the full main rotor using CFD was performed. At first, the rotor was studied in hover, and it was shown that deploying the flaps at high thrust could allow for a small increase of the figure of merit, of less than 1%. This improvement, however, proved limited. Further analyses could focus on deploying one of the flaps, or using different levels of deployment.

The focus was then moved to forward flying rotors, and the whole flight domain of a helicopter

https://doi.org/10.1017/S0001924000011404 Published online by Cambridge University Press

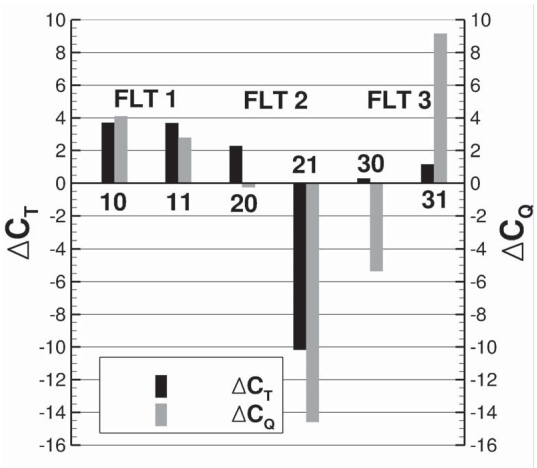

Figure 18. Changes, in percents, of the thrust and torque coefficients in the tested flights with the flaps.

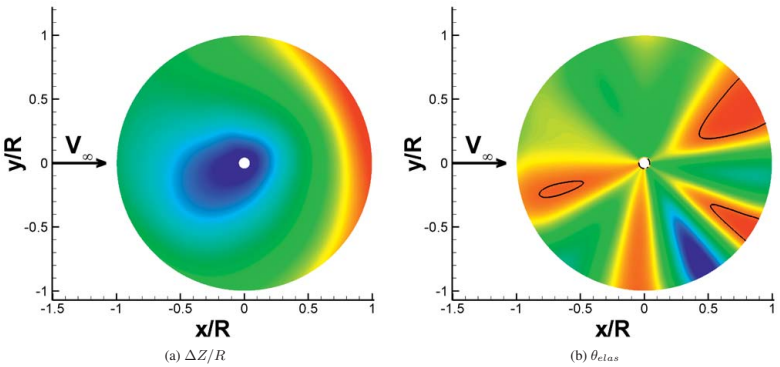

Figure 19. Prescribed deformation to the main rotor blade along the azimuth.

was studied. Despite small differences in the thrust due to trimming, it was highlighted that the flaps proved beneficial at high thrust and high lift, except when, on the retreating side, the blade was already deeply stalled and the flaps could not help recover attached flow. The influence of the flaps on the rotor performance at lower thrust proved, however, limited.

ACKNOWLEDGEMENTS

The financial support via the RTVP project of AgustaWestland and the Business Innovation and Skills Department of UK is gratefully acknowledged.

https://doi.org/10.1017/S0001924000011404 Published online by Cambridge University Press

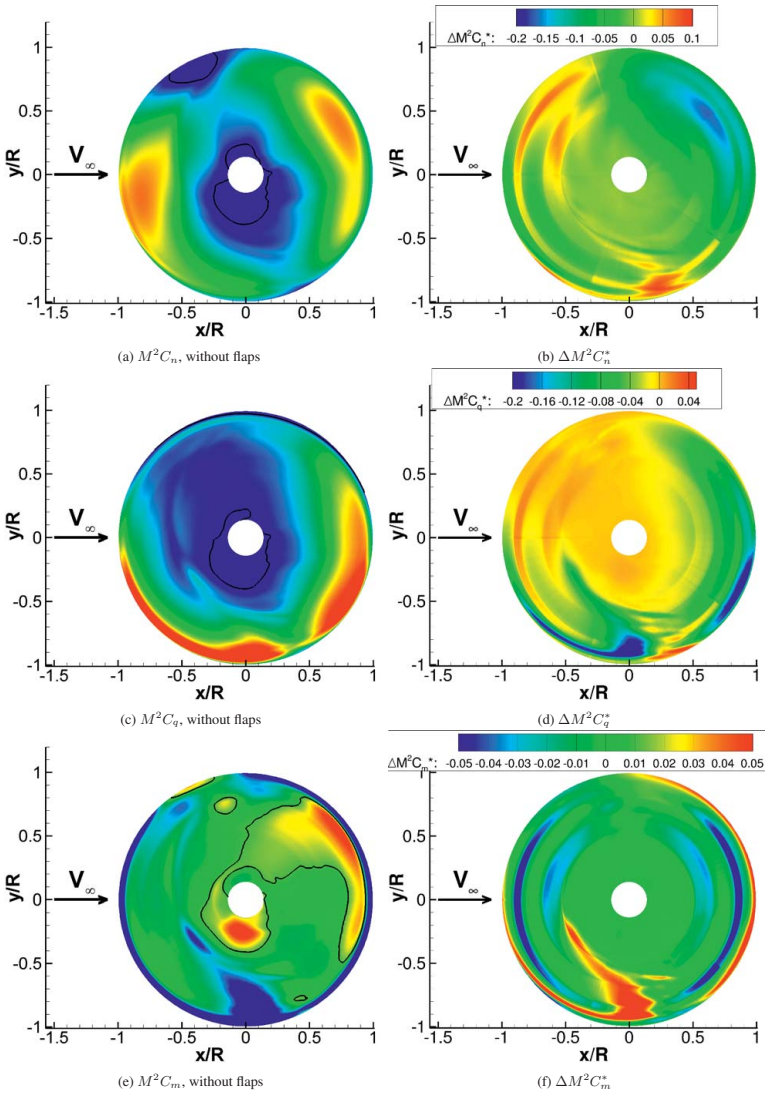

(a) M^2C_n, without flaps (b) $\Delta M^2C_n^*$

(c) M^2C_q, without flaps (d) $\Delta M^2C_q^*$

(e) M^2C_m, without flaps (f) $\Delta M^2C_m^*$

Figure 20. Mach-scaled normal force, torque and moment coefficient predictions for Flight 2-21, using prescribed deformations. Assessment of the effect of the flaps. Prescribed deformations were applied to the blades. In the plots without flaps, thick black lines indicate a value of 0.

REFERENCES

1. BAE, E.S., GANDHI, F. and MAUGHMER, M. Optimally scheduled deployments of miniature Trailing-Edge Effectors for Rotorcraft Power Reduction, American Helicopter Society 65th Annual Forum, 27-29 May 2009, Grapevine, TX, USA.
2. BAE, E.S. and GANDHI, F. Upstream active Gurney flap for rotorcraft vibration reduction, American Helicopter Society 68th Annual Forum, 1-3 May 2012, Fort Worth, TX, USA.
3. PADTHE, A. Simultaneous BVI noise and vibration reduction in rotorcraft using microflaps including the effect of actuator saturation, American Helicopter Society 68th Annual Forum, 1-3 May 2012, Fort Worth, TX, USA.

https://doi.org/10.1017/S0001924000011404 Published online by Cambridge University Press

4. BAUCHAU, O., MIN, B.-Y. and SANKAR, L. A CFD-CSD coupled-analysis of HART-II rotor vibration reduction using Gurney flaps, American Helicopter Society 68th Annual Forum, 11-13 May 2010, Phoenix, AZ, USA.
5. STRAUB, F.K., ANAND, V.R., BIRCHETTE, T.S. and LAU, B.H. SMART rotor development and wind tunnel test, 35th European Rotorcraft Forum, 22-25 September 2009, Hamburg, Germany, Paper No 1200.
6. SIM, B.W., POTSDAM, M., KITAPLIOGLU, C., LEMASURIER, P., LORBER, P. and ANDREWS, J. Localized, non-harmonic active flap motions for low frequency in-plane noise reduction, American Helicopter Society 68th Annual Forum, 1-3 May 2012, Fort Worth, TX, USA.
7. BIRCHETTE, T.S., STRAUB, F.K., BROUWERS, E.W., BUSSOM, R.C. and CENTOLANZA, L.R. Active flap design for an advanced CH-47, American Helicopter Society 69th Annual Forum, 21-23 May 2014, Phoenix, AZ, USA.
8. SAMUSENKO, A., ESAULOV, S. and IVCHIN, V.A. Simulation of helicopter vibration reduction by means of higher harmonics control with the use of flight simulator, 38th European Rotorcraft Forum, 4-6 September 2012, Amsterdam, The Netherlands, Paper No 13.
9. TAMER, A., MUSCARELLO, V., MASARATI, P. and QUARANTA, G. Helicopter vibratory loads and vibrations reduction using higher-harmonic control, 39th European Rotorcraft Forum, 3-5 September 2013, Moscow, Russia, Paper No 37.
10. FOGARTY, D.E., WILBUR, M.L., SEKULA, M.K. and BOYD, D.D. CFD/CSD investigation of BVI noise reduction using higher harmonic active-twist control, 38th European Rotorcraft Forum, 4-6 September 2012, Amsterdam, The Netherlands, Paper No 75.
11. RABOURDIN, A., MAURICE, J.-B., DIETRICH, O. and KONSTANZER, P. Blue pulse active rotor control at Airbus Helicopters – new EC-145 demonstrator & flight test results, American Helicopter Society 70th Annual Forum, 20-22 May 2013, Montréal, Québec.
12. RAVICHANDRAN, K., CHOPRA, I., WAKE, B.E. and HEIN, B. Trailing-edge flaps for rotor performance enhancement and vibration control, *J American Helicopter Soc*, April 2013, **58**, (2), pp 1-13.
13. LÉON, O., HAYDEN, E. and GANDHI, F. Rotorcraft operating envelope expansion using extendable chord sections, American Helicopter Society 65th Annual Forum, 27-29 May 2009, Grapevine, TX, USA.
14. BARAKOS, G., STEIJL, R., BADCOCK, K. AND BROCKELHURST, A. Development of CFD capability for full helicopter engineering analysis, 31st European Rotorcraft Forum, 13-15 September 2005, Florence, Italy.
15. OSHER, S. and CHAKRAVARTHY, S. Upwind schemes and boundary conditions with applications to Euler equations in general geometries. *J Computational Physics*, January-February 1983, **50**, pp 447-481.
16. VAN LEER, B. Towards the ultimate conservative difference scheme. V-A second-order sequel to Godunov's method, *J Computational Physics*, July 1979, **32**, pp 101-136.
17. VAN ALBADA, G.D., VAN LEER, B.B. and ROBERTS, W.W. A comparative study of computational methods in Cosmic Gas Dynamics, *Astronomy and Astrophysics*, April 1982, **108**, (1), pp 76-84.
18. MENTER, F.R. Two-equation eddy-viscosity turbulence models for engineering applications, *AIAA J*, 1994, **32**, (8), pp 1598-1605.
19. AXELSSON, O. *Iterative Solution Methods*, 1994, Cambridge University Press, Cambridge, MA, USA.
20. TICKEL, B. Taking shape in 12.0, *ANSYS Advantage*, 2009, **3**,(1), pp 8-10.
21. STEIJL, R., BARAKOS, G. and BADCOCK, K. A framework for CFD analysis of helicopter rotors in hover and forward flight, *Int J Numerical Methods in Fluids*, 2006, **51**, (8), pp 819-847.
22. STEIJL, R., WOODGATE, M. and BARAKOS, G. CFD Requirements for efficient smart-rotor analysis, 35th European Rotorcraft Forum, 16-18 September 2009, Hamburg, Germany, Paper No 1187.
23. DEHAEZE, F. and BARAKOS, G.N. Mesh deformation method for rotor flows, *J Aircr*, January-February 2012, **49**, (1), pp 82–92.
24. GOURA, G.S.L., BADCOCK, K.J., WOODGATE, M.A. and RICHARDS, B.E. Implicit method for the time marching analysis of flutter, *Aeronaut J*, April 2001, **105**, (1046), pp 199-214.
25. BLOM, F.J. Considerations on the spring analogy, *Int J Numerical Methods in Fluids*, 2000, **32**, pp 647-668.
26. DUBUC, L., CANTARITI, F., WOODGATE, M.A., GRIBBEN, B., BADCOCK, K.J. and RICHARDS, B.E. A grid deformation technique for unsteady flow computations, *Int J Numerical Methods in Fluids*, 2000, **32**, pp 285-311.